

Article

Solvent-Free Synthesis of Nickel Nanoparticles as Catalysts for CO₂ Hydrogenation to Methane

Olga V. Netskina^{1,2,*} , Kirill A. Dmitruk^{1,2}, Alexander A. Paletsky^{1,3}, Svetlana A. Mukha¹, Alena A. Pochtar^{1,2}, Olga A. Bulavchenko¹ , Igor P. Prosvirin¹, Andrey G. Shmakov³, Anna M. Ozerova^{1,4} , Janna V. Veselovskaya^{1,2}, Olga I. Mazina¹ and Oxana V. Komova^{1,4} 

¹ Boreskov Institute of Catalysis SB RAS, Pr. Akademika Lavrentieva 5, 630090 Novosibirsk, Russia

² Department of Natural Sciences, Novosibirsk State University, 1 Pirogova Str., 630090 Novosibirsk, Russia

³ Voevodsky Institute of Chemical Kinetics and Combustion SB RAS, 3 Institutskaya Str., 630090 Novosibirsk, Russia

⁴ Siberian Branch of Russian Academy of Sciences, Pr. Akademika Lavrentieva 17, 630090 Novosibirsk, Russia

* Correspondence: netskina@catalysis.ru; Tel.: +7-383-330-74-58

Abstract: The solid-state combustion method was used to prepare nickel-based catalysts for CO₂ hydrogenation from [Ni(C₃H₄N₂)₆](NO₃)₂ and [Ni(C₃H₄N₂)₆](ClO₄)₂. These complexes were synthesized by adding nickel nitrate and perchlorate to melted imidazole. The composition and structure of the obtained complexes was confirmed by ATR FTIR, powder XRD, and elemental analysis. The stages of thermal decomposition of the complexes and their kinetic parameters were established. It was found that incomplete gasification of more thermostable Ni(C₃H₄N₂)₆(ClO₄)₂ led to the formation of carbon, nitrogen, and chlorine impurities. According to powder XRD and XPS, the solid products of gasification of both complexes consist of NiO and Ni⁰ covered with nickel hydroxide and/or a carbonate layer. In the case of the sample prepared from [Ni(C₃H₄N₂)₆](ClO₄)₂, this layer was pronounced. Therefore, it limits the nickel reduction in the reaction medium of CO₂ hydrogenation, even at 450 °C. The surface of the sample prepared from [Ni(C₃H₄N₂)₆](NO₃)₂ contains nickel oxide, which is easily reduced. So, the catalyst active phase is already formed at 250 °C in the presence of CO₂ and efficiently catalyzes CO₂ hydrogenation as the temperature increases. Therefore, [Ni(C₃H₄N₂)₆](NO₃)₂ is a promising precursor for the CO₂ hydrogenation catalyst, and its solvent-free synthesis follows Green Chemistry principles.

Keywords: solvent-free synthesis; solid-state combustion; nickel; nanoparticle; catalyst; CO₂ methanation



Citation: Netskina, O.V.; Dmitruk, K.A.; Paletsky, A.A.; Mukha, S.A.; Pochtar, A.A.; Bulavchenko, O.A.; Prosvirin, I.P.; Shmakov, A.G.; Ozerova, A.M.; Veselovskaya, J.V.; et al. Solvent-Free Synthesis of Nickel Nanoparticles as Catalysts for CO₂ Hydrogenation to Methane. *Catalysts* **2022**, *12*, 1274. <https://doi.org/10.3390/catal12101274>

Academic Editors: Boxiong Shen and Peng Yuan

Received: 29 September 2022

Accepted: 18 October 2022

Published: 19 October 2022

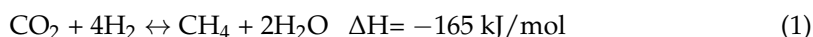
Publisher's Note: MDPI stays neutral with regard to jurisdictional claims in published maps and institutional affiliations.



Copyright: © 2022 by the authors. Licensee MDPI, Basel, Switzerland. This article is an open access article distributed under the terms and conditions of the Creative Commons Attribution (CC BY) license (<https://creativecommons.org/licenses/by/4.0/>).

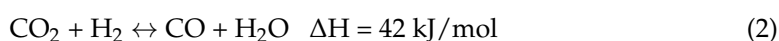
1. Introduction

Global warming on Earth accelerates with the growth of the concentration of greenhouse gases in the atmosphere, such as carbon dioxide (CO₂). Adsorption of CO₂ and its subsequent utilization is one of the solutions to this issue [1,2]. One of the promising ways of recycling CO₂ is its hydrogenation to methane, also known as CO₂ methanation:

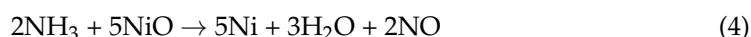
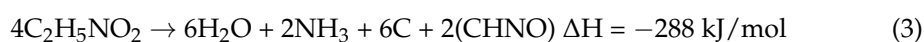


This approach simultaneously solves the task of chemical hydrogen storage [3–5], allows the production of biogas with a higher methane content [6,7], and can be used to remove carbon oxides (CO and CO₂) from hydrogen-rich gas mixtures [8].

According to the thermodynamic calculations [9], the hydrogenation of CO₂ to methane with a high selectivity at atmospheric pressure in a stoichiometric reaction mixture is possible only in the temperature range below 400 °C. At higher temperatures, the reduction of CO₂ to CO is observed.



At temperatures below 400 °C, this process cannot be carried out without catalysts due to the high energy barrier of carbon reduction [10]. Platinum group metals, Ru, Rh, and Pd, show the greatest catalytic activity in the hydrogenation of CO₂ due to their excellent ability to dissociatively adsorb hydrogen, but other transition metals can be used as catalysts as well [3,11–13]. Nickel exhibits a lesser catalytic activity in this process, but due to its low cost, nickel catalysts are widely used in the industry [14,15]. Traditionally, their preparation involves the energy-consuming calcination of the nickel precursor [16]. As a result, nickel oxide is formed, which is reduced to metal in a stream of pure hydrogen immediately before the hydrogenation of CO₂. It is possible to combine the stages of formation of nickel oxide and its reduction to metal in the self-propagating high-temperature synthesis (SHS) using nickel complex compounds as precursors of the active component [17–21]. In the literature [22], this type of SHS is called the solid-state combustion (SSC) method because it involves the high-temperature gasification of solid energy-rich composition. Most often, it is a mixture of nickel nitrate with organic compounds. Since Ni is the active phase of the catalysts in the CO₂ hydrogenation, it is important to use the combustion preparation methods by which the Ni/NiO ratio in the condensed products may be varied. It was noted that nickel oxide is formed during the thermolysis of nickel nitrate [23], but the addition of organic compound (glycine) leads to the reduction of part of nickel ions to the metallic state [24]. In excess of the organic component, the predominant formation of the metal phase is observed [25–30]. It was shown that the thermolysis of nickel complexes with aminoguanidine and semicarbazide also leads to the formation of metallic nickel with an insignificant impurity of nickel oxide [31]. According to [32], the reduction of nickel oxide occurs due to its interaction with ammonia released during the decomposition of nitrogen-containing organic compounds, as, e.g., in the case of glycine [33].



Therefore, it is preferable to use of nitrogen-containing molecules as ligands [29,32,34,35]. If the oxygen- or sulfur-containing compounds are used as organic ligands, then nickel oxide [36,37] or nickel sulfide [38] are formed, respectively. Therefore, the use of these compounds as CO₂ hydrogenation catalysts requires additional reduction with hydrogen.

It should be noted that the aforementioned nickel-containing complexes were obtained using solvents that should be disposed of. It is possible to minimize the ecological impact on the environment through the use of solvent-free methods for the preparation of complexes, which corresponds to the modern concepts of the development of the chemical industry. In this work, we propose a new approach to the synthesis of nickel nitrogen-rich complexes by reacting a nickel salt with melted imidazole, which is thermally stable upon melting [39] and easily forms complex compounds with transition metals. In addition, imidazole is a nitrogen-containing compound, and its decomposition products (ammonia) can reduce nickel cations to a metallic state. Nickel-containing catalysts were obtained from the prepared complexes, which were tested in CO₂ hydrogenation after activation directly in the reaction mixture.

The goals of this work were:

- ✓ To investigate the structure of nickel-containing complexes obtained in the reaction of nickel nitrate and perchlorate with melted imidazole;
- ✓ To study the thermochemical properties of the synthesized nickel-containing complexes;
- ✓ To test the solid products obtained by the SSC method from the synthesized nickel-containing complexes in CO₂ hydrogenation to methane.

2. Results and Discussion

2.1. Synthesis of Nickel Complexes by Melting

Nickel-containing imidazole complexes hexa(imidazole)nickel(II) nitrate $[\text{Ni}(\text{C}_3\text{H}_4\text{N}_2)_6](\text{NO}_3)_2$, and hexa(imidazole)nickel(II) perchlorate $[\text{Ni}(\text{C}_3\text{H}_4\text{N}_2)_6](\text{ClO}_4)_2$ were synthesized as precursors of nickel CO_2 hydrogenation catalysts. They were prepared without the use of solvents, which significantly reduces the preparation time due to the absence of the stage of separating the complexes from solutions and also does not require the further disposal of the solvents. The complexes were synthesized in melted imidazole with nickel nitrate and perchlorate hydrates (Figure 1). Elemental analysis of the samples (Table 1) showed that the resulting compounds contained six imidazole molecules each.

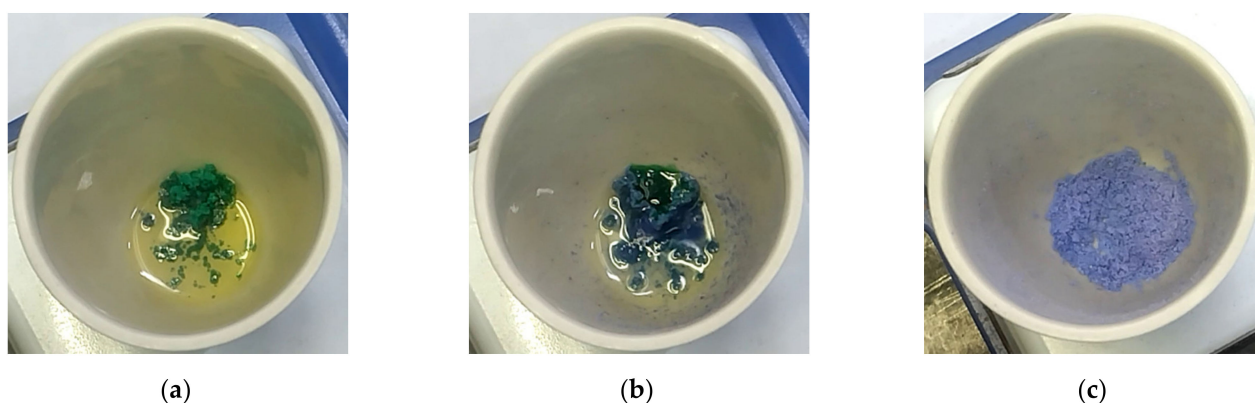


Figure 1. Synthesis of hexa(imidazole)nickel(II) nitrate by adding nickel nitrate to melted imidazole: (a) initial mixture; (b) 1 min; (c) 3 min.

Table 1. Characteristics of the synthesized nickel complexes.

Complex, Molar Mass	Composition, %		Gross Formula	Oxygen Balance, %
	Calculated	Found		
$[\text{Ni}(\text{C}_3\text{H}_4\text{N}_2)_6](\text{NO}_3)_2$ $\text{NiC}_{18}\text{H}_{24}\text{N}_{14}\text{O}_6$ 591 g/mol	Ni—9.9	Ni—9.6	$\text{NiC}_{18.3}\text{H}_{24.6}\text{N}_{14.2}\langle\text{O}\rangle_7$	−116
	C—36.6	C—35.7		
	H—4.1	H—4.0		
	N—33.2	N—32.4		
	O—16.2	Other ($\langle\text{O}\rangle$) ¹ —18.3		
$[\text{Ni}(\text{C}_3\text{H}_4\text{N}_2)_6](\text{ClO}_4)_2$ $\text{NiC}_{18}\text{H}_{24}\text{N}_{12}\text{Cl}_2\text{O}_8$ 666 g/mol	Ni—8.8	Ni—8.7	$\text{NiC}_{18.3}\text{H}_{23.7}\text{N}_{12.4}\text{Cl}_2\langle\text{O}\rangle_{8.2}$	−96
	C—32.5	C—32.3		
	H—3.6	H—3.5		
	N—25.2	N—25.6		
	Cl—10.7	Cl—10.5		
O—19.2	Other ($\langle\text{O}\rangle$) ¹ —19.4			

¹ Supposedly oxygen.

The synthesized complexes were studied by the ATR FTIR spectroscopy method (Figure 2). It can be seen from the ATR FTIR spectra that no structural rearrangements of the imidazole heterocyclic ring occur when imidazole and nickel salts react, but the absorption band of stretching vibrations $\nu(\text{N-H})$ increases in intensity and slightly shifts to the high-frequency region (from 3126 to 3140 cm^{-1} and 3156 cm^{-1} for $[\text{Ni}(\text{C}_3\text{H}_4\text{N}_2)_6](\text{NO}_3)_2$ and $[\text{Ni}(\text{C}_3\text{H}_4\text{N}_2)_6](\text{ClO}_4)_2$, respectively). The metal cation is coordinated by the lone pair of electrons of the pyridine nitrogen atom, breaking the hydrogen bonds between imidazole molecules. In this case, the N-H group becomes more isolated and the distance between atoms shortens. As a result, the absorption bands of stretching vibrations $\nu(\text{N-H})$ are shifted to the high-frequency region. In addition, the obtained compounds do not contain water (Figure 2), since there are no absorption bands near 1600 cm^{-1} , related to the bending vibrations of the water molecules $\delta(\text{H}_2\text{O})$.

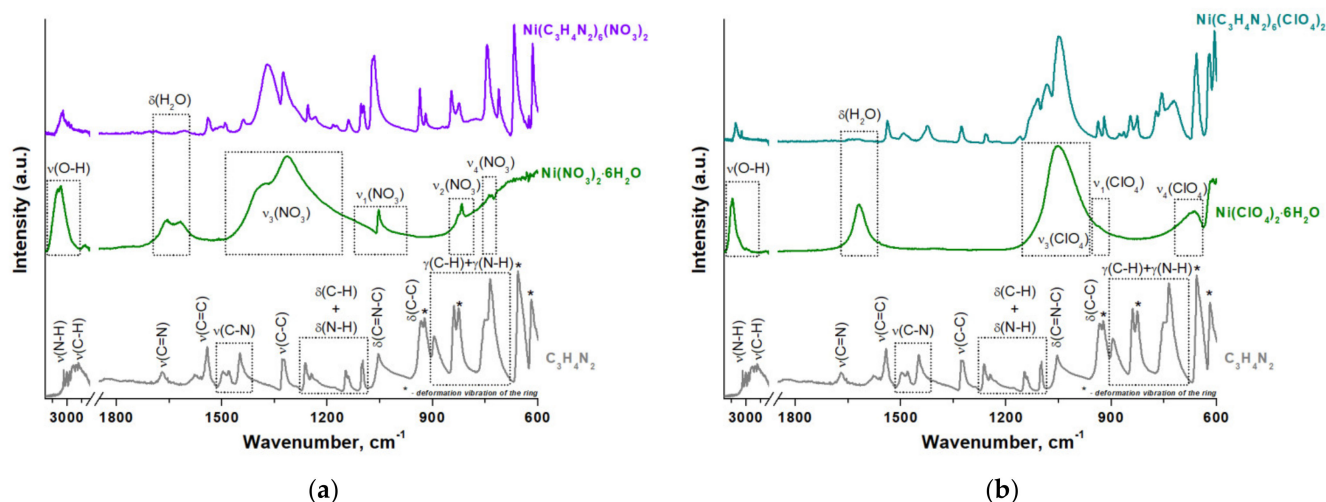


Figure 2. ATR FTIR spectra for synthesized (a) $[\text{Ni}(\text{C}_3\text{H}_4\text{N}_2)_6](\text{NO}_3)_2$ and (b) $[\text{Ni}(\text{C}_3\text{H}_4\text{N}_2)_6](\text{ClO}_4)_2$ complexes (*—deformation vibration of the ring).

The more conclusive evidence of the formation of nickel-containing imidazole complexes during the reaction of nickel salts with melted imidazole was obtained by powder XRD. Thus, the diffraction patterns of the synthesized compounds correspond to the database cards of complexes $[\text{Ni}(\text{C}_3\text{H}_4\text{N}_2)_6](\text{NO}_3)_2$ and $[\text{Ni}(\text{C}_3\text{H}_4\text{N}_2)_6](\text{ClO}_4)_2$ (Figure 3).

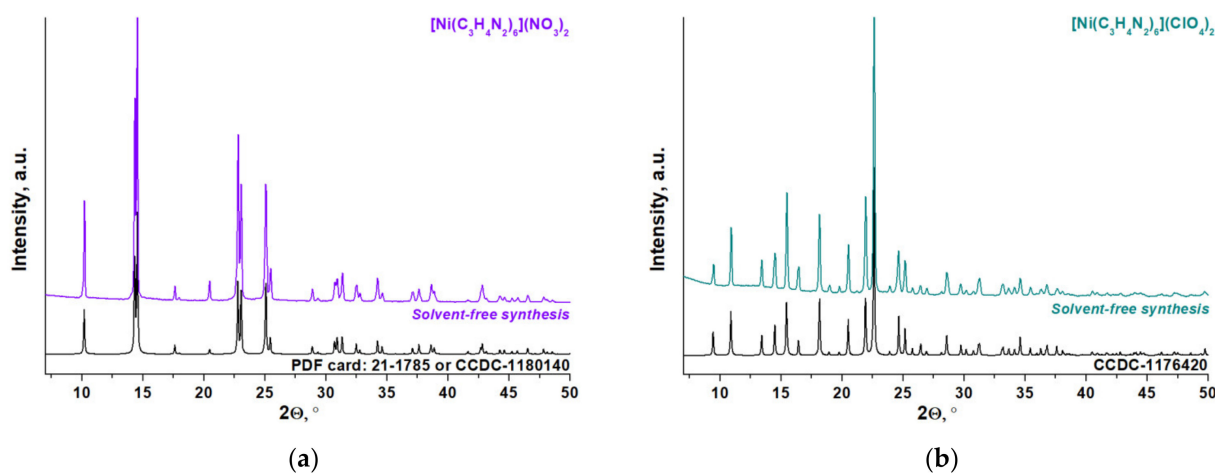


Figure 3. Powder XRD data for synthesized (a) $[\text{Ni}(\text{C}_3\text{H}_4\text{N}_2)_6](\text{NO}_3)_2$ [40] and (b) $[\text{Ni}(\text{C}_3\text{H}_4\text{N}_2)_6](\text{ClO}_4)_2$ [41] complexes.

Thus, a simple energy- and resource-saving solvent-free approach was proposed for the synthesis of nickel-containing imidazole complexes $[\text{Ni}(\text{C}_3\text{H}_4\text{N}_2)_6](\text{NO}_3)_2$ and $[\text{Ni}(\text{C}_3\text{H}_4\text{N}_2)_6](\text{ClO}_4)_2$, which were used as catalyst precursors for CO_2 hydrogenation.

2.2. Thermochemical Properties of the Synthesized Nickel Complexes

The synthesis of catalysts by the SSC method involves the high-temperature decomposition of precursors with the release of a large volume of gases, which ensures a highly dispersed state of the resulting solid product. The thermal analysis data (Figure 4) showed that the thermal decomposition of the synthesized complexes in air begins at 200 °C and has three main stages. The first stage (200–250 °C) is characterized by an endothermic effect and a weight loss of 20 and 18 % for $[\text{Ni}(\text{C}_3\text{H}_4\text{N}_2)_6](\text{NO}_3)_2$ and $[\text{Ni}(\text{C}_3\text{H}_4\text{N}_2)_6](\text{ClO}_4)_2$, respectively. During the second stage (250–300 °C), releasing a large amount of heat and the mass changes by 25% for $[\text{Ni}(\text{C}_3\text{H}_4\text{N}_2)_6](\text{NO}_3)_2$ and 27 % for $[\text{Ni}(\text{C}_3\text{H}_4\text{N}_2)_6](\text{ClO}_4)_2$ are

observed. An exothermic effect is also observed in the third stage at temperatures above 300 °C, but for $[\text{Ni}(\text{C}_3\text{H}_4\text{N}_2)_6](\text{ClO}_4)_2$, it is low-temperature and not a pronounced stage. The total mass loss of $[\text{Ni}(\text{C}_3\text{H}_4\text{N}_2)_6](\text{NO}_3)_2$ and $[\text{Ni}(\text{C}_3\text{H}_4\text{N}_2)_6](\text{ClO}_4)_2$ in air was 86 % and 56 %, respectively.

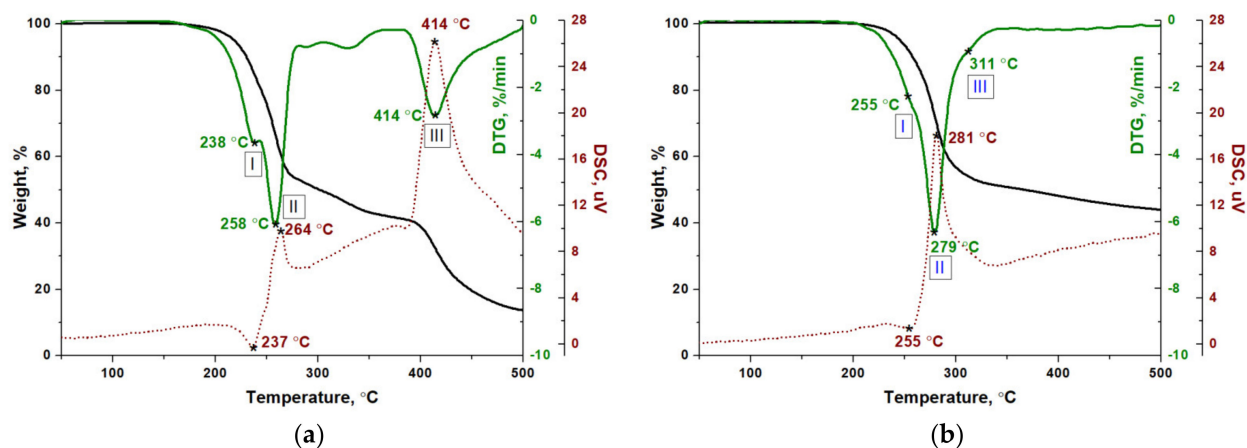


Figure 4. Thermal analysis data for (a) $[\text{Ni}(\text{C}_3\text{H}_4\text{N}_2)_6](\text{NO}_3)_2$ and (b) $[\text{Ni}(\text{C}_3\text{H}_4\text{N}_2)_6](\text{ClO}_4)_2$ complexes prepared by melting-assisted solvent-free synthesis (I, II, III—thermolysis stages). The heating rate in air is 5 °C/min.

According to [42], the first stage of the thermal decomposition of nickel-containing imidazole complexes is an endothermic partial loss of imidazole with its subsequent sublimation. At the second stage, an exothermic redox interaction occurs between imidazole as organic ligand and anions. The third stage can be assigned to the decomposition of the products of incomplete thermolysis of the organic ligand.

The thermal decomposition kinetics of $[\text{Ni}(\text{C}_3\text{H}_4\text{N}_2)_6](\text{NO}_3)_2$ and $[\text{Ni}(\text{C}_3\text{H}_4\text{N}_2)_6](\text{ClO}_4)_2$ complexes were analyzed by the Coats–Redfern method using both traditional linear fitting and the genetic algorithm to find kinetic parameters [43–45]. Figure 5 shows that the second approach more accurately describes the first two stages of decomposition of complexes based on the first-order kinetics, since the obtained coefficients of determination R^2 are higher than 0.999.

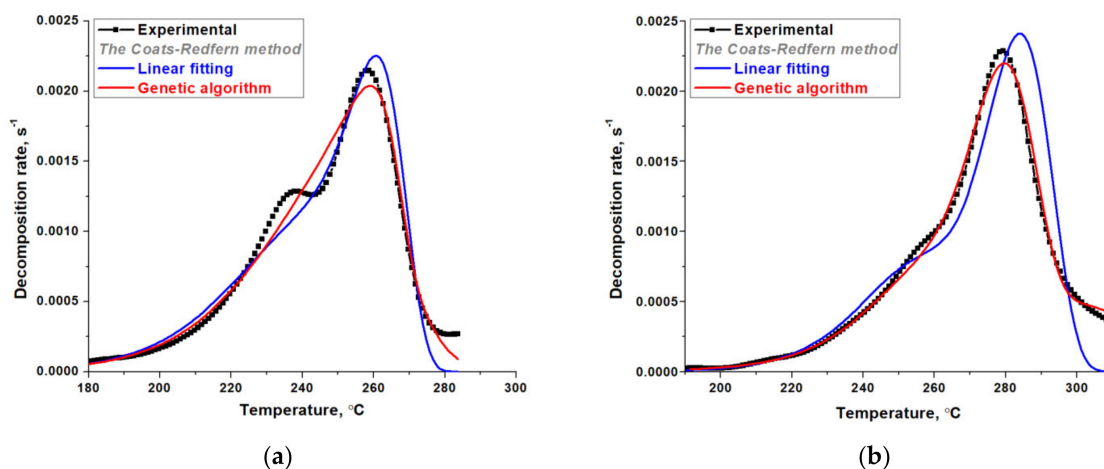


Figure 5. Modelling the thermal decomposition of (a) $[\text{Ni}(\text{C}_3\text{H}_4\text{N}_2)_6](\text{NO}_3)_2$ and (b) $[\text{Ni}(\text{C}_3\text{H}_4\text{N}_2)_6](\text{ClO}_4)_2$ complexes using the Coats–Redfern method. The heating rate in air is 5 °C/min.

As a result of the analysis of the thermal decomposition kinetics by the Coats–Redfern method, the activation energies of the first two stages of decomposition of $[\text{Ni}(\text{C}_3\text{H}_4\text{N}_2)_6](\text{NO}_3)_2$ and $[\text{Ni}(\text{C}_3\text{H}_4\text{N}_2)_6](\text{ClO}_4)_2$ complexes were determined (Table 2).

Table 2. Kinetic parameters of thermal decomposition of $[\text{Ni}(\text{C}_3\text{H}_4\text{N}_2)_6](\text{NO}_3)_2$ and $[\text{Ni}(\text{C}_3\text{H}_4\text{N}_2)_6](\text{ClO}_4)_2$ complexes acquired using the Coats–Redfern method.

Complex	Parameter	Linear Fitting		Genetic Algorithm	
		Stage I	Stage II	Stage I	Stage II
$[\text{Ni}(\text{C}_3\text{H}_4\text{N}_2)_6](\text{NO}_3)_2$	E, kJ/mol	124	284	117	354
	R ²	0.9923	0.9912	0.9995	
$[\text{Ni}(\text{C}_3\text{H}_4\text{N}_2)_6](\text{ClO}_4)_2$	E, kJ/mol	170	255	177	253
	R ²	0.9979	0.9872	0.9999	

The resulting data shows that 117 kJ/mol is required to overcome the energy barrier for the elimination of two imidazole molecules from the complex in the case of the nitrate complex, and 177 kJ/mol in the case of the perchlorate complex. This suggests that imidazole–metal bond in the $[\text{Ni}(\text{C}_3\text{H}_4\text{N}_2)_6](\text{ClO}_4)_2$ complex is stronger.

The second stage of decomposition of the $[\text{Ni}(\text{C}_3\text{H}_4\text{N}_2)_6](\text{NO}_3)_2$ and $[\text{Ni}(\text{C}_3\text{H}_4\text{N}_2)_6](\text{ClO}_4)_2$ complexes is characterized by a significantly higher energy barrier. Thus, the activation energy of the oxidation of imidazole by the nitrate anion is 354 kJ/mol, but the interaction of the perchlorate anion with imidazole has a lower value of 253 kJ/mol and occurs at a high rate almost simultaneously with the first stage. In addition, for the perchlorate-containing complex, significantly more heat is released in the second stage of decomposition than in the case of $[\text{Ni}(\text{C}_3\text{H}_4\text{N}_2)_6](\text{NO}_3)_2$ complex (Figure 4).

The activation energy values (E) obtained by the Coats–Redfern method (genetic algorithm) were used to estimate the critical temperature of thermal explosion for $[\text{Ni}(\text{C}_3\text{H}_4\text{N}_2)_6](\text{NO}_3)_2$ and $[\text{Ni}(\text{C}_3\text{H}_4\text{N}_2)_6](\text{ClO}_4)_2$ complexes, which characterized their thermal stability and safety. For these calculations, DSC data from different heating rates of the complexes in air was obtained (Figure S1). As known, the critical temperature of thermal explosion (T_b) may be calculated using the Tonglai formula [46]:

$$T_b = \frac{E - \sqrt{E^2 - 4ERT_0}}{2R} \quad (5)$$

where R is the molar gas constant and T_0 is the onset temperature at the heating rate of 0 K/min obtained by linear regression.

As the activation energy values depend on the applied method of kinetic analysis of thermogravimetric data the other calculation was also carried out using the Xue formula [47], in which there is no dependence on the activation energy:

$$T_b = T_0 + \frac{\partial T_e}{\partial(\ln \beta)} \quad (6)$$

where T_0 is the onset temperature at the heating rate of 0 K/min, T_e is the onset temperature, and β is the heating rate. The obtained results are summarized in Table 3.

The critical temperatures of thermal explosion for $[\text{Ni}(\text{C}_3\text{H}_4\text{N}_2)_6](\text{NO}_3)_2$ and $[\text{Ni}(\text{C}_3\text{H}_4\text{N}_2)_6](\text{ClO}_4)_2$ complexes obtained by the two methods are close. Their differences do not exceed 10 °C, which indicates that the used method of kinetic analysis was correct. As a result, it was shown that the self-propagating process of thermal decomposition of $[\text{Ni}(\text{C}_3\text{H}_4\text{N}_2)_6](\text{NO}_3)_2$ starts at 242 ± 3 °C and $[\text{Ni}(\text{C}_3\text{H}_4\text{N}_2)_6](\text{ClO}_4)_2$ starts at 254 ± 5 °C. Thus, the synthesized complexes are thermally stable in air, and the thermal decomposition with the release of gaseous products occurs only after reaching a temperature above 230 °C (Figure 4).

Table 3. The critical temperature of thermal explosion for $[\text{Ni}(\text{C}_3\text{H}_4\text{N}_2)_6](\text{NO}_3)_2$ and $[\text{Ni}(\text{C}_3\text{H}_4\text{N}_2)_6](\text{ClO}_4)_2$ complexes.

Complex	β_i , K/min	T_{er} , °C	T_0 , °C	$\frac{\partial(\ln\beta)}{\partial T}$, 1/°C	E, kJ/mol	T_b^1 , °C	T_b^2 , °C
$[\text{Ni}(\text{C}_3\text{H}_4\text{N}_2)_6](\text{NO}_3)_2$	2.5	238.5	239	24	354	245	239
	5	244.6					
	10	266.4					
	20	287.4					
$[\text{Ni}(\text{C}_3\text{H}_4\text{N}_2)_6](\text{ClO}_4)_2$	2.5	259.2	249	21	250	259	249
	5	268.3					
	10	283.6					
	20	302.7					

¹ Tonglai formula; ² Xue formula.

2.3. Thermal Decomposition Mechanism of the Synthesized Nickel Complexes at the High Heating Rates

One of the modern methods for studying the kinetics of thermal decomposition of high-energy material is the analysis of evolved gases by dynamic mass spectrometry [48]. The high sensitivity and instantaneous response of the mass spectrometer make it possible to describe the kinetics of thermal decomposition under conditions of high heating rate (experiment duration is 2 s), which is close to real SSC conditions. In this work, the main gaseous products of the thermal decomposition of $[\text{Ni}(\text{C}_3\text{H}_4\text{N}_2)_6](\text{NO}_3)_2$ and $[\text{Ni}(\text{C}_3\text{H}_4\text{N}_2)_6](\text{ClO}_4)_2$ complexes were identified by this method (Figure 6). It was noted that the composition of the gas and the dynamics of the release of individual products depended on the composition of the complex. Thus, the decomposition products of $[\text{Ni}(\text{C}_3\text{H}_4\text{N}_2)_6](\text{NO}_3)_2$ complex contain imidazole ($m/z = 68$), oxygen ($m/z = 32$), nitrogen oxides—NO ($m/z = 30$) and NO_2 ($m/z = 46$), hydrogen cyanide ($m/z = 27$), carbon dioxide ($m/z = 44$), and nitrogen and/or carbon monoxide ($m/z = 28$). In the gaseous decomposition products of $[\text{Ni}(\text{C}_3\text{H}_4\text{N}_2)_6](\text{ClO}_4)_2$, hydrogen chloride ($m/z = 36$) was identified instead of nitrogen oxides due to the different nature of the anion.

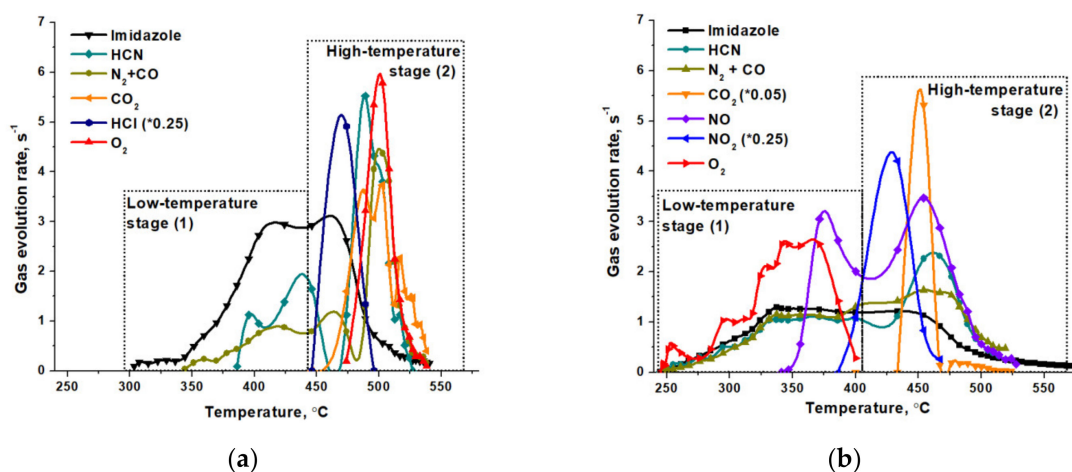


Figure 6. Mass spectrometry of gas released during the thermal decomposition of (a) $[\text{Ni}(\text{C}_3\text{H}_4\text{N}_2)_6](\text{NO}_3)_2$ and (b) $[\text{Ni}(\text{C}_3\text{H}_4\text{N}_2)_6](\text{ClO}_4)_2$ complexes. The heating rate in air is above $100\text{ }^\circ\text{C/s}$ (*0.05 and *0.25—correlation coefficients).

The experimental results were processed using a genetic algorithm to find the kinetic parameters. Since the heating rate could not be maintained constant under the conditions of the highly exothermal decomposition, the comparison function was based on the Arrhenius equation. In this case, the integration was performed numerically under the assumption that the temperature changed uniformly between the experimental points. The

activation energy values obtained for some gaseous products of thermal decomposition of $[\text{Ni}(\text{C}_3\text{H}_4\text{N}_2)_6](\text{NO}_3)_2$ and $[\text{Ni}(\text{C}_3\text{H}_4\text{N}_2)_6](\text{ClO}_4)_2$ complexes are given in Table 4.

Table 4. The kinetic parameters of decomposition of the synthesized nickel complexes at the high heating rates.

Complex	Average Heating Rate, °C/s	Gas (Mass Spectrometer Signal, <i>m/z</i>)	Parameter	Obtained Value	
				Low-Temperature Stage (1)	High-Temperature Stage (2)
$[\text{Ni}(\text{C}_3\text{H}_4\text{N}_2)_6](\text{NO}_3)_2$	245	Imidazole (68)	E, kJ/mol R ²	84	119
		HCN (27)	E, kJ/mol R ²	221	221
		N ₂ + CO (28)	E, kJ/mol R ²	136	63
		O ₂ (32)	E, kJ/mol R ²	99	-
$[\text{Ni}(\text{C}_3\text{H}_4\text{N}_2)_6](\text{ClO}_4)_2$	120	Imidazole (68)	E, kJ/mol R ²	104	264
		HCN (27)	E, kJ/mol R ²	244	323
		N ₂ + CO (28)	E, kJ/mol R ²	246	339
		O ₂ (32)	E, kJ/mol R ²	-	235

Compared with the results of dynamic mass spectral analysis and thermal analysis, we can conclude that the mass loss at the first stage of decomposition of the studied complexes is associated with the successive release of two imidazole molecules. It was found that the activation energy for the removal of the first molecule (Stage 1) is much lower than that of the second (Stage 2), regardless of the composition of the complex. However, imidazole is more easily removed from the nitrate complex than from the perchlorate complex.

From Figure 6, it can be seen that simultaneously with the removal of imidazole molecules from the complex, the following processes are observed: (I) the thermolysis of imidazole with the formation of hydrogen cyanide and (II) the redox interaction of imidazole with anions, which results in the formation of carbon and nitrogen oxides. In addition, the presence of oxygen in the gaseous reaction products confirms the decomposition of anions, accompanied by the release of nitrogen oxides and hydrogen chloride in the case of $[\text{Ni}(\text{C}_3\text{H}_4\text{N}_2)_6](\text{NO}_3)_2$ and $[\text{Ni}(\text{C}_3\text{H}_4\text{N}_2)_6](\text{ClO}_4)_2$ complexes, respectively. All this significantly complicates the description of the kinetics of the decomposition of the complexes, especially in the case of the second stage. Moreover, the rate of these processes depends on the temperature, and on the curves for the release of gaseous products of the thermal decomposition of the complexes, low-temperature (Stage I) and high-temperature (Stage II) regions can be identified. The activation energies determined for these steps (Table 4) indicate higher thermal stability of the $[\text{Ni}(\text{C}_3\text{H}_4\text{N}_2)_6](\text{ClO}_4)_2$ complex in comparison to the $[\text{Ni}(\text{C}_3\text{H}_4\text{N}_2)_6](\text{NO}_3)_2$ complex. This is also consistent with the stability of the perchlorate anion, since its decomposition is observed only in the high-temperature region (Figure 6), and the activation energy value of oxygen evolution is two times higher than that of the nitrate anion. Analyzing the kinetics of oxygen evolution, it should be noted that the obtained values of activation energy are close to the activation energy for the decomposition of nickel nitrate (84 ± 3 kJ/mol) and perchlorate (210 ± 5 kJ/mol) given in [49,50].

Thus, using complementary methods of dynamic mass spectral analysis and thermal analysis, the thermal decomposition of $[\text{Ni}(\text{C}_3\text{H}_4\text{N}_2)_6](\text{NO}_3)_2$ and $[\text{Ni}(\text{C}_3\text{H}_4\text{N}_2)_6](\text{ClO}_4)_2$ complexes was studied. It was shown that the complexes decomposition begins with the successive removal of two imidazole molecules. Simultaneously, the second stage proceeds,

which includes the redox interaction of imidazole with anions, the thermolysis of imidazole, and the decomposition of anions with the release of oxygen.

2.4. Study of Solid Products Obtained by SSC from $\text{Ni}(\text{C}_3\text{H}_4\text{N}_2)_6(\text{NO}_3)_2$ and $[\text{Ni}(\text{C}_3\text{H}_4\text{N}_2)_6](\text{ClO}_4)_2$ Complexes

The aim of gasification of imidazole-containing nickel complexes by the SSC method is to produce solid products. Their highly dispersed state is ensured due to intensive gas evolution. In our work, Ni/NiO-NO₃-SSC and Ni/NiO-ClO₄-SSC samples were obtained from $[\text{Ni}(\text{C}_3\text{H}_4\text{N}_2)_6](\text{NO}_3)_2$ and $[\text{Ni}(\text{C}_3\text{H}_4\text{N}_2)_6](\text{ClO}_4)_2$ complexes, respectively. The phase composition of solid products of the combustion of complexes was studied by powder XRD. It was shown that the Ni/NiO-NO₃-SSC and Ni/NiO-ClO₄-SSC samples contain two phases (Figure 7): metallic nickel—Ni⁰ (PDF 04-0850) and its oxide—NiO (PDF 47-1049). Nickel oxide is the main phase (Table 5), but its content is lower in the sample obtained from the nitrate complex.

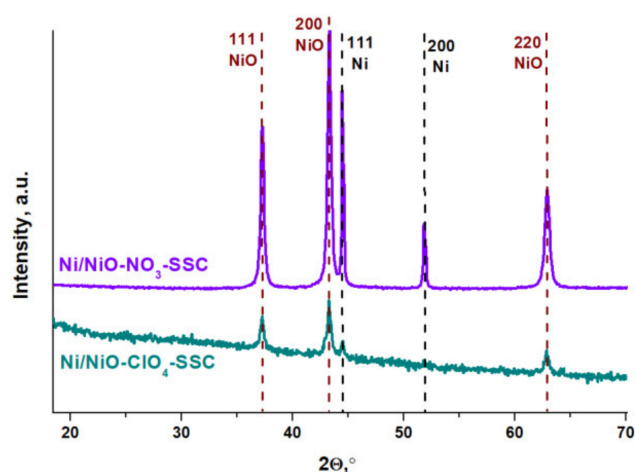


Figure 7. X-ray powder diffraction for Ni/NiO-NO₃-SSC and Ni/NiO-ClO₄-SSC.

Table 5. Powder XRD data for the solid products of $[\text{Ni}(\text{C}_3\text{H}_4\text{N}_2)_6](\text{NO}_3)_2$ and $[\text{Ni}(\text{C}_3\text{H}_4\text{N}_2)_6](\text{ClO}_4)_2$ combustion.

Sample	Phase	Content, wt%	SCR Size from Lvol-IB/Lvol-FWHM, nm
Ni/NiO-NO ₃ -SSC	NiO	80	20 ± 1/26 ± 1
	Ni	20	59 ± 5/74 ± 7
Ni/NiO-ClO ₄ -SSC	NiO	85	20 ± 1/28 ± 2
	Ni	15	24 ± 6/33 ± 8

The CSR width was used to determine the size of crystallites for each phase (Table 5) contained in the decomposition products of $[\text{Ni}(\text{C}_3\text{H}_4\text{N}_2)_6](\text{NO}_3)_2$ and $[\text{Ni}(\text{C}_3\text{H}_4\text{N}_2)_6](\text{ClO}_4)_2$ complexes. The size of nickel oxide crystallites is the same for Ni/NiO-NO₃-SSC and Ni/NiO-ClO₄-SSC. Metallic nickel obtained from the perchlorate complex is more dispersed, since its CSR is two times lower than that of Ni/NiO-NO₃-SSC.

It should be noted that the reduced form of nickel is absent on the surface of Ni/NiO-NO₃-SSC and Ni/NiO-ClO₄-SSC according to the XPS data (Figure 8a). So, the peak at 853 eV in the Ni2p_{3/2} XPS spectra corresponding to Ni⁰ [51] was not found. Under SSC conditions, oxygen in the air probably interacts with the surface of the formed metal particles, oxidizing them to NiO [52] and Ni(OH)₂ [53]. Moreover, the Ni2p_{3/2} peak with a binding energy of 855.8 eV can be attributed not only to nickel hydroxide, but also to nickel carbonate [54] formed due to the reaction between the generated gases and the obtained

nickel-containing phases. Apparently, these compounds are amorphous, since they were not detected by powder XRD (Figure 7).

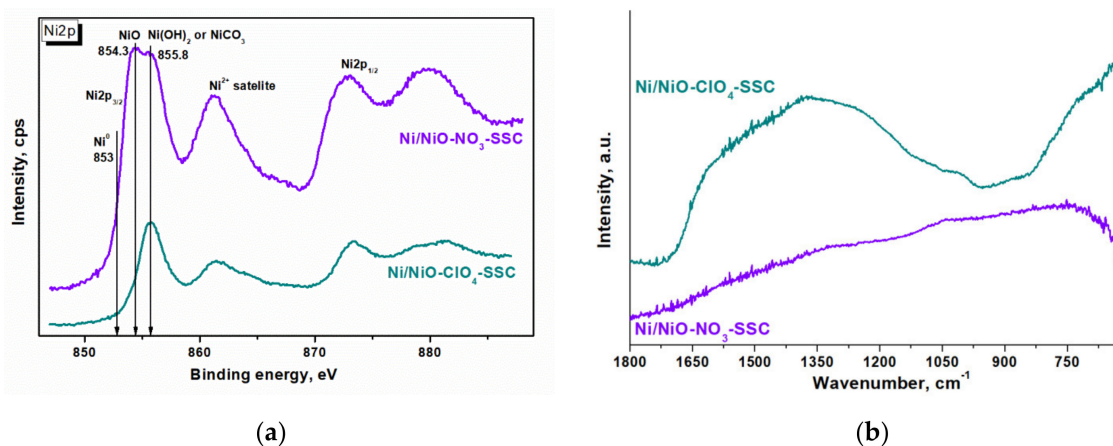


Figure 8. (a) XPS and (b) ATR FTIR spectra for Ni/NiO-NO₃-SSC and Ni/NiO-ClO₄-SSC samples.

In addition to this, the analysis of the XPS survey spectra (Figure S2) shows that not only nickel and oxygen, but also impurities of carbon and nitrogen are present on the surface of Ni/NiO-NO₃-SSC and Ni/NiO-ClO₄-SSC (Table 6). Despite the greater value of the oxygen balance (Table 1), their content is higher in the sample obtained from the perchlorate complex. Furthermore, it contains more than 8 at.% chlorine.

Table 6. XPS data for the solid products of [Ni(C₃H₄N₂)₆](NO₃)₂ and [Ni(C₃H₄N₂)₆](ClO₄)₂ combustion.

Sample	Content, at.% ¹				
	Ni	O	C	N	Cl
Ni/NiO-NO ₃ -SSC	24.6	37.1	35.8	2.5	-
Ni/NiO-ClO ₄ -SSC	7.5	14.3	56.6	13.2	8.3

¹ Atomic percentages.

The higher content of impurities in Ni/NiO-ClO₄-SSC is also confirmed by ATR FTIR spectroscopy, since it is characterized by intense structureless absorption, reaching the highest values in the regions of 1100–1600 cm⁻¹ and 600–800 cm⁻¹ (Figure 8b). Taking into account the elemental composition of impurities (Table 6) and thermal stability of the [Ni(C₃H₄N₂)₆](ClO₄)₂ complex (Tables 2 and 3), absorption in the region of 1100–1600 cm⁻¹ can be attributed to the vibrations of -C-C- and -C-N- bonds with carbon atoms in sp³ hybridization and the stretching vibrations of double bonds -C=C- and -C=N- with carbon atoms in sp² hybridization, according to [55,56]. Structureless absorption in the region of 600–800 cm⁻¹ corresponds to bending vibrations of C-H and N-H groups, including those in heterocyclic compounds [57]. Thus, on the surface of Ni/NiO-ClO₄-SSC there are products of incomplete decomposition of imidazole. These include amorphous carbon or carbon nitride, which are characterized by structureless absorption in the regions of 1100–1600 cm⁻¹ and 600–800 cm⁻¹ [58]. However, the presence of nickel carbonate in the sample is not excluded, since the absorption bands of stretching vibrations of the CO₃ group are also in the region of 1400–1500 cm⁻¹ [59,60].

Summing up the study of the solid products obtained by the combustion of [Ni(C₃H₄N₂)₆](NO₃)₂ and [Ni(C₃H₄N₂)₆](ClO₄)₂ complexes, it can be concluded that the [Ni(C₃H₄N₂)₆](NO₃)₂ complex provides samples with a lower content of impurities. Its surface contains three times more nickel in oxidized form compared to Ni/NiO-ClO₄-SSC (Table 6). The probable cause may be coverage of the nickel-containing phase by the products of incom-

plete decomposition of the $[\text{Ni}(\text{C}_3\text{H}_4\text{N}_2)_6](\text{ClO}_4)_2$ complex, which is more thermally stable than the $[\text{Ni}(\text{C}_3\text{H}_4\text{N}_2)_6](\text{NO}_3)_2$ complex (Figure 4).

2.5. Testing the Solid Products of Nickel Complexes Decomposition in the CO_2 Hydrogenation

The catalytic properties of the Ni/NiO- NO_3 -SSC and Ni/NiO- ClO_4 -SSC samples prepared by SSC from the $[\text{Ni}(\text{C}_3\text{H}_4\text{N}_2)_6](\text{NO}_3)_2$ and $[\text{Ni}(\text{C}_3\text{H}_4\text{N}_2)_6](\text{ClO}_4)_2$ complexes were investigated in the CO_2 hydrogenation to methane. Traditionally, the catalysts are activated at 400–500 °C in a pure hydrogen flow to reduce the active component to the metallic state Ni^0 [61–63], which catalyzes the carbon dioxide–hydrogen interaction [64]. The absence of this standard step is a distinctive feature of our work. The Ni/NiO- NO_3 -SSC and Ni/NiO- ClO_4 -SSC was activated in the flow of the reaction mixture ($\text{H}_2:\text{CO}_2:\text{Ar} = 16:4:80$), which is more efficient from a practical point of view. The reduction of the samples was monitored by FTIR spectroscopy of the gas phase at the outlet of the reactor. The appearance of the absorption bands in the 2900–3000 cm^{-1} range, corresponding to the stretching vibrations of the C-H bonds in the methane molecule [65] indicates the beginning of catalyst activation.

When testing the Ni/NiO- NO_3 -SSC and Ni/NiO- ClO_4 -SSC samples, the temperature in the reactor was increased from 25 to 450 °C. It was noted that in the presence of Ni/NiO- NO_3 -SSC methane began to form at 250 °C, and its contribution to gaseous products increased significantly at higher temperatures (Figure 9a). In the case of Ni- ClO_4 -SSC, the absorption bands of methane were detected only at 350 °C (Figure 9b), and their amount changed little with increasing the temperature up to 450 °C. This is due to significantly lower CO_2 conversion compared to the Ni/NiO- NO_3 -SSC sample (Figure 10).

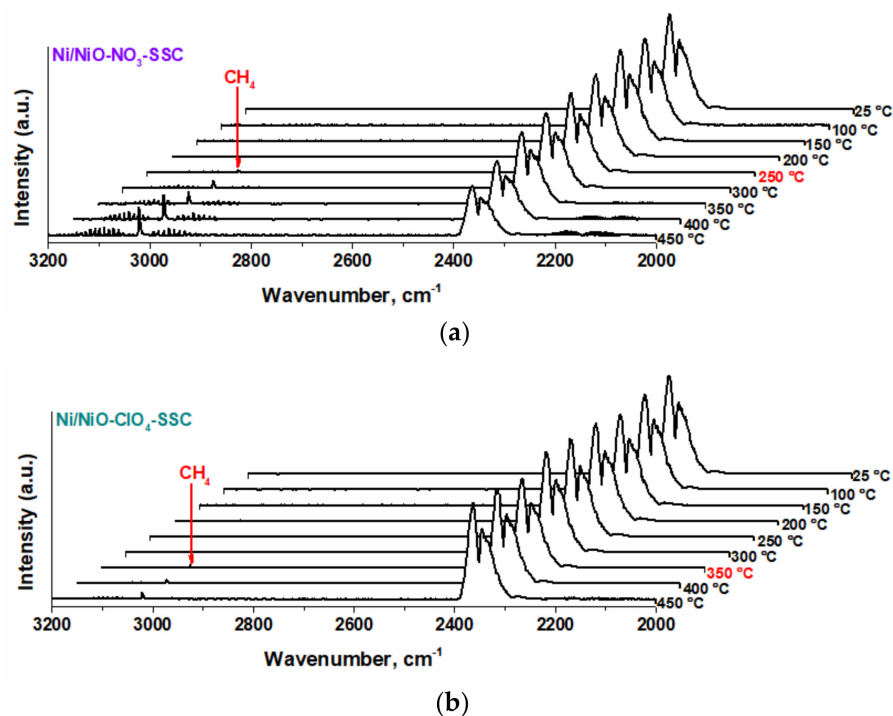


Figure 9. FTIR spectra of gases at the outlet of the reactor during the activation of (a) Ni/NiO- NO_3 -SSC and (b) Ni/NiO- ClO_4 -SSC at different temperatures in the reaction medium. Activation conditions: volume ratio is $\text{H}_2:\text{CO}_2:\text{Ar} = 16:4:80$, hourly mass feed flow rate is $19,000 \text{ cm}^3 \cdot \text{g}_{\text{cat}}^{-1} \cdot \text{h}^{-1}$.

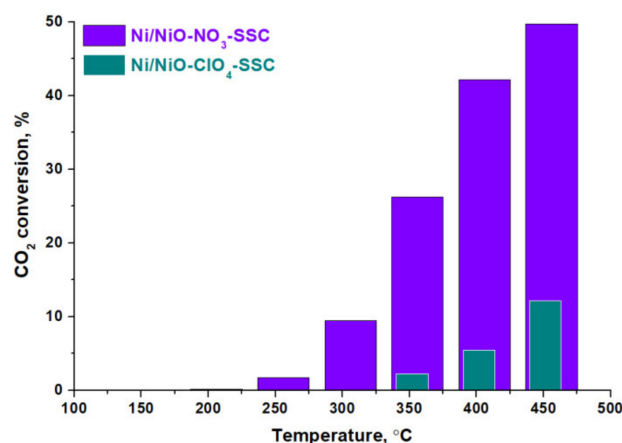


Figure 10. CO₂ conversion during the activation of Ni/NiO-NO₃-SSC and Ni/NiO-ClO₄-SSC at different temperatures in the reaction medium (H₂:CO₂:Ar = 16:4:80).

To determine the reason for such a large difference in activation temperatures, the activated Ni/NiO-NO₃-SSC and Ni/NiO-ClO₄-SSC samples were studied by the XPS method. From Figure 11, it can be seen that both catalysts contain the reduced form of nickel on the surface after activation at 450 °C. Deconvolution of the Ni2p_{3/2} peak revealed that the Ni⁰/Ni²⁺ molar ratio for Ni/NiO-NO₃-SSC is 0.65, but it is only 0.2 for Ni/NiO-ClO₄-SSC.

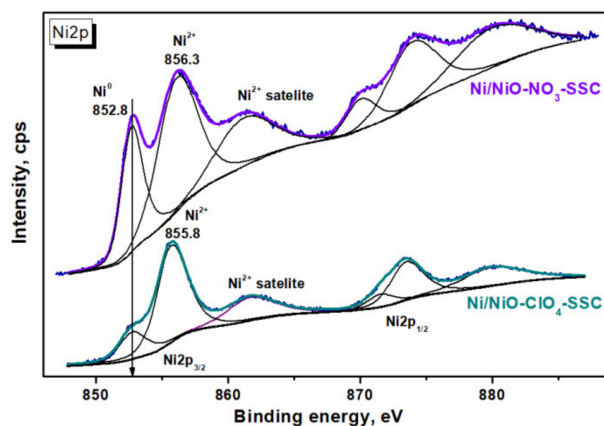


Figure 11. Deconvoluted XPS spectra of Ni/NiO-NO₃-SSC and Ni/NiO-ClO₄-SSC samples after activation at 450 °C in the reaction medium (H₂:CO₂:Ar = 16:4:80).

Such an insignificant reduction of nickel at 450 °C in the case of Ni/NiO-ClO₄-SSC can be attributed to two reasons. First, impurities on the Ni/NiO-ClO₄-SSC surface can prevent the access of hydrogen to the nickel-containing phase. Secondly, the reduction of nickel hydroxide occurs in a higher temperature range [66]:



Thus, it is more preferable to use the [Ni(C₃H₄N₂)₆](NO₃)₂ complex as the precursor of the active phase of the CO₂ hydrogenation catalyst. In addition, the Ni/NiO-NO₃-SSC catalyst from this complex is activated at a lower temperature in the presence of CO₂ than the industrial NIAP-07-01 catalyst [67].

3. Experimental Details

3.1. Materials

For the synthesis of nickel complexes, the following reagents were used: Ni(NO₃)₂·6H₂O (GOST 4055-70, 98%); Ni(ClO₄)₂·6H₂O (TU 6-09-02-118-86, 98%); imidazole—C₃H₄N₂ (CAS 288-32-4, 99%).

3.2. Complex Synthesis

[Ni(C₃H₄N₂)₆](NO₃)₂ In order to synthesize the complex compound, nickel (II) nitrate (0.01 mol) was added to melted imidazole (0.06 mol) at 90 °C and stirred. The reaction mixture became purple and then quickly crystallized as a powder with a yield of 97%. After that, the sample was stored in a desiccator over P₂O₅.

[Ni(C₃H₄N₂)₆](ClO₄)₂ In order to synthesize the complex compound, nickel (II) perchlorate (0.01 mol) was added to melted imidazole (0.06 mol) at 90 °C and stirred. The reaction mixture became cornflower-colored and then quickly crystallized as a powder with a yield of 95%. After that, the sample was stored in a desiccator over P₂O₅.

3.3. Synthesis of Nickel Catalysts by Solid-State Combustion Method

In order to synthesize nickel catalysts, powders of complexes were placed in a corundum crucible and preheated on the IKA-C-Mag HS4 hot plate (IKA, Königswinter, Germany) with the heating temperature set to 500 °C. The samples melted followed by spontaneous gasification within a few minutes, leaving black powder in the crucible. The powder was granulated, and a fraction with the particle size of 0.25–0.5 mm was prepared for testing in catalytic experiments and stored in a desiccator over P₂O₅.

The solid products of combustion of the [Ni(C₃H₄N₂)₆](NO₃)₂ and [Ni(C₃H₄N₂)₆](ClO₄)₂ complexes are denoted by Ni/NiO-NO₃-SSC and Ni/NiO-ClO₄-SSC, respectively.

3.4. Characterization of Complexes and Solid Products of Combustion

3.4.1. Composition of Complexes and Products of Their Thermolysis

The Ni content was found by inductively coupled plasma atomic emission spectrometry on an Optima 4300 DV (PerkinElmer, Waltham, MA, USA). The carbon, hydrogen, and nitrogen contents were determined using an automatic CHNS analyzer EURO EA 3000 (Euro Vector S.p.A., Castellanza, Italy). In the analyzer, the complexes (0.5–2 mg) were combusted in a vertical reactor at 1050 °C in a flow of He with added O₂. The measurement error was in the range of ±3%.

Oxygen balance was calculated based on the determined C, H, N, and Ni contents using the following equation:

$$\text{Oxygen balance (\%)} = \frac{-1600}{\text{Molar mass}} \cdot (2C + \frac{H}{2} + M - O) \quad (9)$$

where *C* is the quantity of carbon atoms, *H* is the quantity of hydrogen atoms, *O* is the quantity of oxygen atoms, and *M* is the quantity of metal atoms.

The X-ray powder diffraction (XRD) patterns of the synthesized nickel complexes and solid products of their combustion were acquired using a D8 Advance diffractometer equipped with a Lynxeye linear detector (Bruker AXS GmbH, Karlsruhe, Germany). The powder XRD patterns were obtained in the 2θ range from 5 to 70° with a step of 0.05° and accumulation time of 2 s using CuK_α radiation (λ = 1.5418 Å). The composition of the solid-state combustion products was determined by the Rietveld method [68] using the TOPAS program (TOPAS—Total Pattern Analysis System, Version 4.2, Bruker AXS). The reference material for describing the instrumental broadening was metallic silicon. The size of the coherent scattering region (CSR) was calculated using LVol-IB (LVol-IB—the volume-weighted mean column height based on integral breadth) and LVol-FWHM (the volume-weighted mean column height based on full width at half maximum, k = 0.89) values. Crystallographic data for the complexes have been deposited with the Cambridge Crystallographic Data Centre, CCDC, 12 Union Road, Cambridge CB21EZ,

UK. Copies of the data can be obtained free of charge by quoting the depository numbers: CCDC-1180140 for $[\text{Ni}(\text{C}_3\text{H}_4\text{N}_2)_6](\text{NO}_3)_2$; CCDC-1176420 for $[\text{Ni}(\text{C}_3\text{H}_4\text{N}_2)_6](\text{ClO}_4)_2$ (<http://www.ccdc.cam.ac.uk>, accessed on 1 September 2022). Theoretical powder pattern for $[\text{Ni}(\text{C}_3\text{H}_4\text{N}_2)_6](\text{NO}_3)_2$ and $[\text{Ni}(\text{C}_3\text{H}_4\text{N}_2)_6](\text{ClO}_4)_2$ plotted from the CIF available in [40] and [41], respectively.

Infrared spectra of the complexes and solid products of combustion were obtained by attenuated total reflection infrared spectroscopy (ATR FTIR) using an Agilent Cary 630 spectrometer (Agilent Technologies, Santa Clara, CA, USA) equipped with a Gladi ATR attachment (PIKE Technologies, Madison, WI, USA).

A SPECS photoelectron spectrometer with a PHOIBOS-150-MCD-9 hemispheric analyzer and a FOCUS-500 monochromator (SPECS Surface Nano Analysis GmbH, Berlin, Germany) (AlK_{α} radiation, 150 W, $h\nu = 1486.74$ eV) was used to record X-ray photoelectron spectra (XPS) of the solid products of combustion. The samples were transported and supported on a conducting scotch in an inert atmosphere (argon) to prevent oxidation of the particle surface in air during storage. The binding energy (BE) scale of the spectrometer was precalibrated using $\text{Au}4f_{7/2}$ (84.0 eV) and $\text{Cu}2p_{3/2}$ (932.6 eV) core-level peaks. The measurement error was ± 0.1 eV. The sample charge was taken into account using C1s lines (284.8 eV). Individual spectra of elements were used to calculate the composition of the surface while accounting for element sensitivity coefficients [69].

3.4.2. Study of Thermochemical Properties of Nickel Complexes

The thermal decomposition of nickel complexes (5 mg) was studied using a Netzsch STA 449 C Jupiter instrument equipped with a DSC/TG holder (NETZSCH, Selb, Germany) in the temperature range of 30–500 °C under a flow of air ($30 \text{ mL} \cdot \text{min}^{-1}$) with the heating rate of $5 \text{ }^\circ\text{C} \cdot \text{min}^{-1}$. Based on the TG-DSC data, the kinetic parameters of the main two stages of the thermal decomposition of the complexes were determined using the traditional Coats–Redfern method with linear fitting [70] and the Coats–Redfern method with the genetic algorithm to find the pre-exponential factor and activation energy. Within the framework of this approach, the rate of the thermal decomposition reaction is written [71] as

$$\frac{d\alpha}{dt} = A e^{-\frac{E}{RT}} (1 - \alpha)^n \quad (10)$$

where t is time, α is the conversion degree (or portion of decomposed compound), $\frac{d\alpha}{dt}$ is the reaction rate, A is the pre-exponential factor, E is the activation energy, R is the gas constant, T is temperature, and n is the reaction order.

Taking into account the heating rate $\beta = \frac{dT}{dt}$, Equation (10) was integrated:

$$\int_0^{\alpha} \frac{d\alpha}{(1 - \alpha)^n} = \frac{A}{\beta} \int_{T_0}^T e^{-\frac{E}{RT}} dT \text{ or } -\ln(1 - \alpha) = \frac{ART^2}{\beta E} \left[1 - \frac{2RT}{E} \right] e^{-\frac{E}{RT}} \quad (n = 1) \quad (11)$$

Using this equation, the kinetic parameters were calculated. For the estimation of the efficiency of modeling the experimental data, it is necessary to introduce a fitness function (F) [72]. In this study the fitness function (12) was applied.

$$F = \frac{1}{N} \sum_i \left(\frac{1}{2} (\alpha_i^{\text{theor}} - \alpha_i^{\text{exper}})^2 + \left(\frac{1}{2} \left(\frac{\alpha^{\text{theor}}}{dt_i} - \frac{\alpha^{\text{exper}}}{dt_i} \right)^2 \right) \right) \quad (12)$$

where N represents the number of experimental points, i is the value of the experimental point at some temperature α_i^{theor} and α_i^{exper} are theoretical and experimental values of the portion of decomposed compound at some temperature, $\frac{\alpha^{\text{theor}}}{dt_i}$ and $-\frac{\alpha^{\text{exper}}}{dt_i}$ are theoretical and experimental values of reaction rate at some temperature. The search for activation energy and the pre-exponential factor of each stage was performed in ranges of 50–550 kJ/mol and 104 – 1040 s^{-1} , respectively.

The TG-DSC data at a different heating rate (2.5, 5, 10, 20 °C/min) and the activation energy obtained by the genetic algorithm were used to estimate the critical temperature of thermal explosion for the complexes by methods described by Tonglai et al. [46] and Xue et al. [47].

The composition of gaseous products of combustion was analyzed by the dynamic mass-spectral thermal analysis (DMSTA) method, using a time-of-flight mass spectrometer with a molecular beam sampling system MSCh-4 (Plant Of Scientific Instrumentation, Sumy, USSR) under a flow of Ar (5 mL·min⁻¹). Average heating rate ranged from 100 to 245 °C·s⁻¹. The sample weight was 1–5 mg. The delay between measurements was 0.04 s. The identification of mass spectral signals was carried out using the mass spectra of individual substances from the NIST database.

Kinetic parameters of separated stages of the thermal decomposition of the complexes under high heating rate were found by the genetic algorithm based on mass-spectral signals with *m/z* of 68 and 32. The search for activation energy and the pre-exponential factor of each stage was performed in ranges of 50–550 kJ/mol and 10⁴–10⁴⁰ s⁻¹, respectively. However, since the heating rate could not be maintained consistent during the combustion, the Coats–Redfern method for integrating the reaction rate equation could not be used. Thus, Equation (10) was integrated numerically to acquire α_i^{theor} for the fitting function.

3.5. Experimental Setup for Studying CO₂ Hydrogenation

Experimental investigation of the catalytic properties of nickel complexes and solid products of combustion was carried out in a fixed-bed reactor (inner diameter—12.8 mm) at atmospheric pressure. The catalyst load was 318 mg. The reactor was heated in a tubular furnace, and the temperature was controlled using a thermocouple installed in the catalytic bed. The temperature varied from 150 to 450 °C with a step of 50 °C. The temperature was increased every 20 min until catalyst activation was observed, and afterwards the duration of each step varied.

The flow of the reaction mixture (H₂:CO₂:Ar = 16:4:80) passed through the catalytic bed with an hourly mass feed flow rate of 19.000 mL·g_{cat}⁻¹·h⁻¹. The flow rate was controlled by an RRG-12-36 flow meter (“Eltochpribor”, Moscow, Russia) with an accuracy of 1%. The composition of the gas at the reactor’s outlet was determined using an Agilent Cary 630 FTIR-spectrometer (Agilent Technologies Australia, Melbourne, Australia) with the gas cell’s internal volume of 100 cm³ and the optical path length of 10 cm.

The amount of CO₂ in the reaction medium before and after the reactor was determined using nondispersive infrared sensors (Dynamment Limited, Mansfield, UK). The obtained data were used to calculate CO₂ (X_{CO₂}) conversion as follows:

$$X_{CO_2} = \left(1 - \frac{C_{out}}{C_{in}} \cdot \frac{U_{out}}{U_{in}}\right) \cdot 100\% \quad (13)$$

where *C_{in}* and *C_{out}* are CO₂ concentrations at the inlet and outlet of the reactor, and *U_{in}* and *U_{out}* are gas flow rates at the inlet and outlet of the reactor. Taking into account reaction stoichiometry (the reaction proceeds with a decrease in volume) and the high content of argon in the reaction medium, the *U_{in}*/*U_{out}* ratio was in the range from 0.92 to 1.

4. Conclusions

Using a solvent-free melting-assisted method, [Ni(C₃H₄N₂)₆](NO₃)₂ and [Ni(C₃H₄N₂)₆](ClO₄)₂ complexes were prepared as precursors of CO₂ hydrogenation catalysts. Their composition and structure were confirmed by elemental analysis, ATR FTIR, and powder XRD. The thermochemical properties of the complexes were studied, and it was shown that [Ni(C₃H₄N₂)₆](ClO₄)₂ is more thermally stable due to the stronger imidazole–metal interactions and the thermal stability of the perchlorate anion. That is one of the reasons for the lower degree of its gasification in the SSC conditions, because the resulting solid product contains carbon, nitrogen, and chlorine impurities. There are far fewer impurities in the solid product of [Ni(C₃H₄N₂)₆](NO₃)₂ thermal decomposition. It was found by powder

XRD that nickel oxide and reduced nickel are the main components of the solid products of gasification of the $[\text{Ni}(\text{C}_3\text{H}_4\text{N}_2)_6](\text{NO}_3)_2$ and $[\text{Ni}(\text{C}_3\text{H}_4\text{N}_2)_6](\text{ClO}_4)_2$ complexes. However, XPS showed that the particles' surface is covered by an amorphous layer of hydroxide and/or carbonate nickel, which is pronounced in the case of the sample prepared from $[\text{Ni}(\text{C}_3\text{H}_4\text{N}_2)_6](\text{ClO}_4)_2$. This led to a lower degree of nickel reduction ($\text{Ni}^0/\text{Ni}^{2+} = 0.2$) during the catalysts activation in the CO_2 hydrogenation reaction medium, even at 450°C . Nickel oxide on the surface of the sample prepared from $[\text{Ni}(\text{C}_3\text{H}_4\text{N}_2)_6](\text{NO}_3)_2$ ensures the formation of metallic nickel ($\text{Ni}^0/\text{Ni}^{2+} = 0.65$) already at 250°C in the presence of CO_2 , which efficiently catalyzes the interaction of CO_2 and hydrogen with further temperature increases.

As a result, $[\text{Ni}(\text{C}_3\text{H}_4\text{N}_2)_6](\text{NO}_3)_2$ is a more promising precursor for CO_2 hydrogenation catalyst. It provides a lower impurity level in solid products of gasification, a large fraction of reduced metal, and a formation of nickel oxide on the particle surface, which reduces to the catalytically active phase even at 250°C in the CO_2 presence. It should be noted that the activation of industrial catalysts for CO_2 hydrogenation to methane begins only at temperatures over 350°C under similar conditions, as established in our previous studies [67].

Supplementary Materials: The following supporting information can be downloaded at: <https://www.mdpi.com/article/10.3390/catal12101274/s1>, Figure S1: DSC data for $[\text{Ni}(\text{C}_3\text{H}_4\text{N}_2)_6](\text{NO}_3)_2$ and $[\text{Ni}(\text{C}_3\text{H}_4\text{N}_2)_6](\text{ClO}_4)_2$ complexes at different heating rates; Figure S2: XPS survey spectra for Ni/NiO- NO_3 -SSC and Ni/NiO- ClO_4 -SSC.

Author Contributions: Conceptualization, O.V.N. and O.V.K.; methodology, S.A.M., J.V.V. and K.A.D.; formal analysis, A.G.S. and A.A.P. (Alexander A. Paletsky); investigation, A.M.O., K.A.D., A.A.P. (Alena A. Pochtar), I.P.P., O.I.M. and O.A.B.; data curation, A.A.P. (Alexander A. Paletsky), S.A.M., I.P.P., O.A.B. and A.A.P. (Alena A. Pochtar); writing—original draft preparation, K.A.D., O.I.M. and A.M.O.; writing—review and editing, O.V.K. and A.G.S.; supervision, J.V.V.; project administration, O.V.N. All authors have read and agreed to the published version of the manuscript.

Funding: This research was funded by the Ministry of Science and Higher Education of the Russian Federation (project no. 075-15-2020-781).

Data Availability Statement: Not applicable.

Conflicts of Interest: The authors declare no conflict of interest.

References

1. Younas, M.; Sohail, M.; Leong, L.K.; Bashir, M.J.K.; Sumathi, S. Feasibility of CO_2 adsorption by solid adsorbents: A review on low-temperature systems. *Int. J. Environ. Sci. Technol.* **2016**, *13*, 1839–1860. [CrossRef]
2. Younas, M.; Kong, L.L.; Bashir, M.J.K.; Nadeem, H.; Shehzad, A.; Sethupathi, S. Recent Advancements, Fundamental Challenges, and Opportunities in Catalytic Methanation of CO_2 . *Energy Fuels* **2016**, *30*, 8815–8831. [CrossRef]
3. Fan, W.K.; Tahir, M. Recent trends in developments of active metals and heterogenous materials for catalytic CO_2 hydrogenation to renewable methane: A review. *J. Environ. Chem. Eng.* **2021**, *9*, 105460. [CrossRef]
4. Kuznecova, I.; Gusca, J. Property based ranking of CO and CO_2 methanation catalysts. *Energy Procedia* **2017**, *128*, 255–260. [CrossRef]
5. Lee, W.J.; Li, C.; Prajitno, H.; Yoo, J.; Patel, J.; Yang, Y.; Lim, S. Recent trend in thermal catalytic low temperature CO_2 methanation: A critical review. *Catal. Today* **2021**, *368*, 2–19. [CrossRef]
6. Jensen, M.B.; Ottosen, L.D.M.; Kofoed, M.V.W. H_2 gas-liquid mass transfer: A key element in biological Power-to-Gas methanation. *Renew. Sustain. Energy Rev.* **2021**, *147*, 111209. [CrossRef]
7. Ren, J.; Liu, Y.-L.; Zhao, X.-Y.; Cao, J.-P. Methanation of syngas from biomass gasification: An overview. *Int. J. Hydrogen Energy* **2020**, *45*, 4223–4243. [CrossRef]
8. Takenaka, S.; Shimizu, T.; Otsuka, K. Complete removal of carbon monoxide in hydrogen-rich gas stream through methanation over supported metal catalysts. *Int. J. Hydrogen Energy* **2004**, *29*, 1065–1073. [CrossRef]
9. Gao, J.; Wang, Y.; Ping, Y.; Hu, D.; Xu, G.; Gu, F.; Su, F. A thermodynamic analysis of methanation reactions of carbon oxides for the production of synthetic natural gas. *RSC Adv.* **2012**, *2*, 2358–2368. [CrossRef]
10. Vogt, C.; Monai, M.; Sterk, E.B.; Palle, J.; Melcherts, A.E.M.; Zijlstra, B.; Groeneveld, E.; Berben, P.H.; Boereboom, J.M.; Hensen, E.J.M.; et al. Understanding carbon dioxide activation and carbon-carbon coupling over nickel. *Nat. Commun.* **2019**, *10*, 5330. [CrossRef]

11. Debek, R.; Azzolina-Jury, F.A.; Travert, A.; Maugéa, F. A review on plasma-catalytic methanation of carbon dioxide—Looking for an efficient catalyst. *Renew. Sustain. Energy Rev.* **2019**, *116*, 109427. [[CrossRef](#)]
12. Hussain, I.; Jalil, A.A.; Hassan, N.S.; Hamid, M.Y.S. Recent advances in catalytic systems for CO₂ conversion to substitute natural gas (SNG): Perspective and challenges. *J. Energy Chem.* **2021**, *62*, 377–407. [[CrossRef](#)]
13. Su, X.; Xu, J.; Liang, B.; Duan, H.; Hou, B.; Huang, Y. Catalytic carbon dioxide hydrogenation to methane: A review of recent studies. *J. Energy Chem.* **2016**, *25*, 553–565. [[CrossRef](#)]
14. Aziz, M.A.A.; Jalil, A.A.; Triwahyono, S.; Ahmad, A. CO₂ methanation over heterogeneous catalysts: Recent progress and future prospects. *Green Chem.* **2015**, *17*, 2647–2663. [[CrossRef](#)]
15. Lv, C.; Xu, L.; Chen, M.; Cui, Y.; Wen, X.; Li, Y.; Wu, C.; Yang, B.; Miao, Z.; Hu, X.; et al. Recent progresses in constructing the highly efficient ni based catalysts with advanced low-temperature activity toward CO₂ methanation. *Front. Chem.* **2020**, *8*, 269. [[CrossRef](#)]
16. Efremov, V.N.; Golosman, E.Z.; Kashinskaya, A.V.; Mugenov, T.I.; Zolotareva, V.E.; Polivanov, B.I.; Polushin, A.P. Resistance of industrial nickel-containing methanation catalysts to the poisoning by organic carbon dioxide absorbents. *Chim. Techno Acta* **2017**, *4*, 167–182. [[CrossRef](#)]
17. Jiang, Y.; Huang, T.; Dong, L.; Qin, Z.; Ji, H. Ni/bentonite catalysts prepared by solution combustion method for CO₂ methanation. *Chin. J. Chem. Eng.* **2018**, *26*, 2361–2367. [[CrossRef](#)]
18. Italiano, C.; Llorca, J.; Pino, L.; Ferraro, M.; Antonucci, V.; Vita, A. CO and CO₂ methanation over Ni catalysts supported on CeO₂, Al₂O₃ and Y₂O₃ oxides. *Appl. Catal. B Environ.* **2020**, *264*, 118494. [[CrossRef](#)]
19. Summa, P.; Gajewska, M.; Li, L.; Hu, C.; Samojeden, B.; Motak, M.; Da Costa, P. Solution combustion synthesis as an alternative synthesis route for novel Ni-Mg-Al mixed-oxide catalyst for CO₂ methanation. *J. CO₂ Util.* **2022**, *60*, 101983. [[CrossRef](#)]
20. Shafiee, P.; Alavi, S.M.; Rezaei, M. Mechanochemical synthesis method for the preparation of mesoporous Ni–Al₂O₃ catalysts for hydrogen purification via CO₂ methanation. *J. Energy Inst.* **2021**, *96*, 1–10. [[CrossRef](#)]
21. Shafiee, P.; Alavi, S.M.; Rezaei, M. Solid-state synthesis method for the preparation of cobalt doped Ni–Al₂O₃ mesoporous catalysts for CO₂ methanation. *Int. J. Hydrogen Energy* **2021**, *46*, 3933–3944. [[CrossRef](#)]
22. Parauha, Y.R.; Sahu, V.; Dhoble, S.J. Prospective of combustion method for preparation of nanomaterials: A challenge. *Mater. Sci. Eng. B* **2021**, *267*, 115054. [[CrossRef](#)]
23. Brockner, W.; Ehrhardt, C.; Gjikaj, M. Thermal decomposition of nickel nitrate hexahydrate, Ni(NO₃)₂·6H₂O, in comparison to Co(NO₃)₂·6H₂O and Ca(NO₃)₂·4H₂O. *Thermochim. Acta* **2007**, *456*, 64–68. [[CrossRef](#)]
24. Deraz, N.M. Magnetic behavior and physicochemical properties of Ni and NiO nano-particles. *Curr. Appl. Phys.* **2012**, *12*, 928–934. [[CrossRef](#)]
25. Erri, P.; Nader, J.; Varma, A. Controlling Combustion Wave Propagation for Transition Metal/Alloy/Cermet Foam Synthesis. *Adv. Mater.* **2008**, *20*, 1243–1245. [[CrossRef](#)]
26. Jung, C.-H.; Jalota, S.; Bhaduri, S.B. Quantitative effects of fuel on the synthesis of Ni/NiO particles using a microwave-induced solution combustion synthesis in air atmosphere. *Mater. Lett.* **2005**, *59*, 2426–2432. [[CrossRef](#)]
27. Khaliullin, S.M.; Zhuravlev, V.D.; Bamburov, V.G.; Khort, A.A.; Roslyakov, S.I.; Trusov, G.V.; Moskovskikh, D.O. Effect of the residual water content in gels on solution combustion synthesis temperature. *J. Sol-Gel Sci. Technol.* **2020**, *93*, 251–261. [[CrossRef](#)]
28. Su, Q.; Wang, X.J.; Shu, Q.H.; Chen, S.S.; Jin, S.H.; Li, L.J. Synthesis, Crystal Structure, and Properties of Energetic Complexes Constructed from Transition Metal Cations (Fe, Co, Cu, and Pb) and BTO²⁻. *J. Heterocycl. Chem.* **2017**, *54*, 3227–3234. [[CrossRef](#)]
29. Xanthopoulou, G.; Thoda, O.; Roslyakov, S.; Steinman, A.; Kovalev, D.; Levashov, E.; Vekinis, G.; Sytschev, A.; Chronos, A. Solution combustion synthesis of nano-catalysts with a hierarchical structure. *J. Catal.* **2018**, *364*, 112–124. [[CrossRef](#)]
30. Guo, Q.; Zhao, Y.; Liu, J.; Ma, C.; Zhou, H.; Chen, L.; Huang, B.; Wei, W. Novel solid metal–organic self-propagation combustion for controllable synthesis of hierarchically porous metal monoliths. *J. Mater. Chem. A* **2015**, *3*, 10179–10182. [[CrossRef](#)]
31. Gavrilov, A.I.; Tukhtaev, R.K.; Larionov, S.V.; Lavrenova, L.G.; Savel'eva, Z.A.; Boldyrev, V.V. Preparation of dispersed nickel with controlled morphology by combustion process. *Dokl. Akad. Nauk.* **1996**, *348*, 201–204.
32. Kumar, A.; Wolf, E.E.; Mukasyan, A.S. Solution combustion synthesis of metal nanopowders: Nickel—Reaction pathways. *AIChE J.* **2011**, *57*, 2207–2214. [[CrossRef](#)]
33. Weiss, I.M.; Muth, C.; Drumm, R.; Kirchner, H.O.K. Thermal decomposition of the amino acids glycine, cysteine, aspartic acid, asparagine, glutamic acid, glutamine, arginine and histidine. *BMC Biophys.* **2018**, *11*, 2. [[CrossRef](#)] [[PubMed](#)]
34. Manukyan, K.V.; Cross, A.; Roslyakov, S.; Rouvimov, S.; Rogachev, A.S.; Wolf, E.E.; Mukasyan, A.S. Solution Combustion Synthesis of Nano-Crystalline Metallic Materials: Mechanistic Studies. *J. Phys. Chem. C* **2013**, *117*, 24417–24427. [[CrossRef](#)]
35. Kumar, A.; Wolf, E.E.; Mukasyan, A.S. Solution combustion synthesis of metal nanopowders: Copper and copper/nickel alloys. *AIChE J.* **2011**, *57*, 3473–3479. [[CrossRef](#)]
36. Salehi, M.; Galini, M.; Kubicki, M.; Khaleghian, A. Synthesis and characterization of new cobalt(III) and nickel(II) complexes derived from acetylacetone and 2-aminopyridine: A new precursor for preparation of NiO nanoparticles. *Russ. J. Inorg. Chem.* **2019**, *64*, 18–27. [[CrossRef](#)]
37. Salavati-Niasari, M.; Davar, F.; Fereshteh, Z. Synthesis of nickel and nickel oxide nanoparticles via heat-treatment of simple octanoate precursor. *J. Alloys Compd.* **2010**, *494*, 410–414. [[CrossRef](#)]
38. Sivasankar, B.N.; Ragunath, L. Thermal degradation kinetics of Co(II), Ni(II), and Zn(II) hydrazinesulfonates in air, oxygen and nitrogen atmospheres. *Thermochim. Acta* **2003**, *397*, 237–247. [[CrossRef](#)]

39. Grimmett, M.R. Advances in Imidazole Chemistry. *Adv. Heterocycl. Chem.* **1970**, *12*, 103–183.
40. Santoro, A.; Mighell, A.D.; Zocchi, M.; Reimann, C.W. The crystal and molecular structure of hexakis(imidazole)nickel(II) nitrate ($C_3H_4N_2$)₆Ni(NO₃)₂. *Acta Cryst.* **1969**, *B25*, 842–847. [[CrossRef](#)]
41. Ivarsson, G.J.M.; Forsling, W. The structure of hexakis(imidazole)nickel(II) diperchlorate. *Acta Cryst.* **1979**, *B35*, 1896–1897. [[CrossRef](#)]
42. Gomm, P.S.; Underhill, A.E.; Oliver, R.W.A. Thermal decomposition of imidazole complexes of the type MIm_6X_2 (where $M = Co$ or Ni ; $X = Cl, Br, \text{ or } I$; $Im = C_3H_4N_2$ and $M = Co$; $X = NO_3$). *J. Inorg. Nucl. Chem.* **1972**, *34*, 1879–1883. [[CrossRef](#)]
43. Richter, F.; Rein, G. Pyrolysis kinetics and multi-objective inverse modelling of cellulose at the microscale. *Fire Saf. J.* **2017**, *91*, 191–199. [[CrossRef](#)]
44. Rein, G.; Lautenberger, C.; Fernandez-Pello, A.C.; Torero, J.L.; Urban, D.L. Application of genetic algorithms and thermogravimetry to determine the kinetics of polyurethane foam in smoldering combustion. *Combust. Flame* **2006**, *146*, 95–108. [[CrossRef](#)]
45. Korobeinichev, O.P.; Paletsky, A.A.; Gonchikzhapov, M.B.; Shundrina, I.K.; Chen, H.; Liu, N. Combustion Chemistry and Decomposition Kinetics of Forest Fuels. *Procedia Eng.* **2013**, *62*, 182–193. [[CrossRef](#)]
46. Tonglai, Z.; Rongzu, H.; Yi, X.; Fuping, L. The estimation of critical temperatures of thermal explosion for energetic materials using non-isothermal DSC. *Thermochim. Acta* **1994**, *244*, 171–176. [[CrossRef](#)]
47. Xue, L.; Zhao, F.Q.; Hu, R.Z.; Gao, H.X. A Simple Method to Estimate the Critical Temperature of Thermal Explosion for Energetic Materials Using Nonisothermal DSC. *J. Energ. Mater.* **2010**, *28*, 17–34. [[CrossRef](#)]
48. Kamruddin, M.; Ajikumar, P.K.; Dash, S.; Purniah, B.; Tyagi, A.K.; Krishan, K. Evolved gas analysis by mass spectrometry. *Instrum. Sci. Technol.* **1995**, *23*, 123–135. [[CrossRef](#)]
49. Criado, J.M.; Ortega, A.; Real, C. Mechanism of the thermal decomposition of anhydrous nickel nitrate. *React. Solids.* **1987**, *4*, 93–103. [[CrossRef](#)]
50. Solymosi, F.; Raskó, J. Study of the thermal decompositions of some transition metal perchlorates. *J. Therm. Anal.* **1977**, *11*, 289–304. [[CrossRef](#)]
51. Chen, S.; Zhang, Y.; Li, Y.; Liu, W.; Song, Y.; Wang, L. Porous Carbon Derived from Petals of Yulan Magnolia Doped with Ni and NiO as Anodes for Lithium Ion Battery. *Int. J. Electrochem. Sci.* **2019**, *14*, 1926–1939. [[CrossRef](#)]
52. Chen, X.; Honda, K.; Zhang, Z.-G. CO₂ single bond CH₄ reforming over NiO/ γ -Al₂O₃ in fixed/fluidized-bed multi-switching mode. *Appl. Catal. A-Gen.* **2005**, *279*, 263–271. [[CrossRef](#)]
53. Biesinger, M.C.; Lau, L.W.M.; Gerson, A.R.; Smart, R.S.C. The role of the Auger parameter in XPS studies of nickel metal, halides and oxides. *Phys. Chem. Chem. Phys.* **2012**, *14*, 2434–2442. [[CrossRef](#)] [[PubMed](#)]
54. Ji, Y.; Ma, M.; Ji, X.; Xiong, X.; Sun, X. Nickel-carbonate nanowire array: An efficient and durable electrocatalyst for water oxidation under nearly neutral conditions. *Front. Chem. Sci. Eng.* **2018**, *12*, 467–472. [[CrossRef](#)]
55. Chu, P.K.; Li, L. Characterization of amorphous and nanocrystalline carbon films. *Mater. Chem. Phys.* **2006**, *96*, 253–277. [[CrossRef](#)]
56. Rodil, S.E. Infrared spectra of amorphous carbon based materials. *Diam. Relat. Mater.* **2005**, *14*, 1262–1269. [[CrossRef](#)]
57. Madanagopal, A.; Periandy, S.; Gayathri, P.; Ramalingam, S.; Xavier, S.; Ivanov, V.K. Spectroscopic and computational investigation of the structure and pharmacological activity of 1-benzylimidazole. *J. Taibah Univ. Sci.* **2017**, *11*, 975–996. [[CrossRef](#)]
58. Ferrari, A.C.; Rodil, S.E.; Robertson, J.; Rodil, S.E.; Robertson, J. Interpretation of infrared and Raman spectra of amorphous carbon nitrides. *Phys. Rev. B-Condens. Matter Mater. Phys.* **2003**, *67*, 1553061–15530620. [[CrossRef](#)]
59. Minkova, N.; Krusteva, M.; Nikolov, G. Spectroscopic study of nickel hydroxyde, nickel carbonate-hexahydrate and nickel hydroxocarbonate. *J. Mol. Struct.* **1984**, *115*, 23–26. [[CrossRef](#)]
60. Li, Q.; Liu, D.; Chen, C.; Shao, Z.; Wang, H.; Liu, J.; Zhang, Q.; Gadd, G.M. Experimental and geochemical simulation of nickel carbonate mineral precipitation by carbonate-laden ureolytic fungal culture supernatants. *Environ. Sci. Nano* **2019**, *6*, 1866. [[CrossRef](#)]
61. Darouhegi, R.; Meshkani, F.; Rezaei, M. Enhanced activity of CO₂ methanation over mesoporous nanocrystalline Ni–Al₂O₃ catalysts prepared by ultrasound-assisted co-precipitation method. *Int. J. Hydrogen Energy* **2017**, *42*, 15115–15125. [[CrossRef](#)]
62. Rahmani, S.; Rezaei, M.; Meshkani, F. Preparation of highly active nickel catalysts supported on mesoporous nanocrystalline γ -Al₂O₃ for CO₂ methanation. *J. Ind. Eng. Chem.* **2014**, *20*, 1346–1352. [[CrossRef](#)]
63. Liang, C.; Tian, H.; Guo, G.; Zhang, S.; Liu, Q.; Dong, D.; Hu, X. Methanation of CO₂ over alumina supported nickel or cobalt catalysts: Effects of the coordination between metal and support on formation of the reaction intermediates. *Int. J. Hydrogen Energy* **2020**, *45*, 531–543. [[CrossRef](#)]
64. Pan, Q.; Peng, J.; Sun, T.; Wang, S.; Wang, S. Insight into the reaction route of CO₂ methanation: Promotion effect of medium basic sites. *Catal. Commun.* **2014**, *45*, 74–78. [[CrossRef](#)]
65. Dinu, D.F.; Podewitz, M.; Grothe, H.; Loerting, T.; Liedl, K.R. Decomposing anharmonicity and mode-coupling from matrix effects in the IR spectra of matrix-isolated carbon dioxide and methane. *Phys. Chem. Chem. Phys.* **2020**, *22*, 17932–17947. [[CrossRef](#)]
66. Sreenavya, A.; Baskaran, T.; Ganesh, V.; Sharma, D.; Nagendra, K.; Sakthivel, A. Framework of ruthenium-containing nickel hydrotalcite-type material: Preparation, characterisation, and its catalytic application. *RSC Adv.* **2018**, *8*, 25248–25257.
67. Netskina, O.V.; Mucha, S.S.; Veselovskaya, J.V.; Bolotov, V.A.; Komova, O.V.; Ishchenko, A.V.; Bulavchenko, O.A.; Prosvirin, I.P.; Pochtar, A.A.; Rogov, V.A. CO₂ methanation: Nickel-alumina catalyst prepared by solid-state combustion. *Materials* **2021**, *14*, 6789. [[CrossRef](#)]

68. Rietveld, H.M. A profile refinement method for nuclear and magnetic structures. *J. Appl. Crystallogr.* **1969**, *2*, 65–71. [[CrossRef](#)]
69. Scofield, J.H. Hartree-Slater subshell photoionization cross-sections at 1254 and 1487 eV. *J. Electron Spectrosc. Relat. Phenom.* **1976**, *8*, 129–137. [[CrossRef](#)]
70. Coats, A.W.; Redfern, J.P. Kinetic parameters from thermogravimetric data. *Nature* **1964**, *201*, 68–69. [[CrossRef](#)]
71. Adenson, M.O.; Adenson, M.O.; Kelley, M.D.; Elkelany, O.O.; Biernacki, J.J.; Liu, Y.-W. Kinetics of cellulose pyrolysis: Ensuring optimal outcomes. *Can. J. Chem. Eng.* **2018**, *96*, 926–935. [[CrossRef](#)]
72. Purnomo, D.M.J.; Richter, F.; Bonner, M.; Vaidyanathan, R.; Rein, G. Role of optimisation method on kinetic inverse modelling of biomass pyrolysis at the microscale. *Fuel* **2020**, *262*, 116251. [[CrossRef](#)]